Optics Communications 281 (2008) 4273–4281

Contents lists available at ScienceDirect

Optics Communications

journal homepage: www.elsevier.com/locate/optcom

Common-path phase-shifting digital holographic microscopy: A way to quantitative phase imaging and superresolution

Vicente Mico [a,*], Zeev Zalevsky [b], Javier García [c]

[a] AIDO, Technological Institute of Optics, Colour and Imaging, C/Nicolás Copérnico, 7-13 Parc Tecnològic, 46980 Paterna, (Valencia), Spain
[b] School of Engineering, Bar-Ilan University, Ramat-Gan 52900, Israel
[c] Departamento de Óptica, Universitat de València, C/Dr. Moliner, 50, 46100 Burjassot, Spain

ARTICLE INFO

Article history:
Received 26 December 2007
Received in revised form 23 April 2008
Accepted 29 April 2008

Keywords:
Quantitative phase imaging
Digital holographic microscopy
Phase-shifting techniques
Synthetic aperture microscopy
Fourier image formation
Superresolution

ABSTRACT

We present an experimental setup useful for complex amplitude evaluation and phase image quantification of three-dimensional (3-D) samples in digital holographic microscopy (DHM). It is based on a common-path interferometric configuration performed by dividing the input plane in two contiguous regions and by placing a translation grating near to the Fourier plane. Then, complex amplitude distribution of the sample under test is recovered with phase-shifting standard method obtained by moving the grating using a linear motion stage. Some experimental results of an USAF resolution test are presented for different numerical aperture (NA) microscope lenses. In a second part, the proposed setup is tested under superresolution purposes. Based on the object's spectrum shift produced by off-axis illumination, we use time multiplexing to generate a synthetic aperture enlargement that improves the final image resolution. Experimental results for the case of a biosample (human red blood cells) and a commercial low NA microscope lens validates the suggested superresolution approach.

1. Introduction

Visualization and characterization of an object's complex amplitude distribution is an open and highly attractive topic in applied optics. As examples, many contributions have been presented along the years in fields such as phase object imaging [1–5], wavefront and phase aberration sensing [6–10], and characterization of flow turbulences [11–14]. Anyway, quantitative and/or qualitative phase determination becomes the starting point of any involved analysis. But due to fact that phase distribution can not be imaged directly, additional methods are needed to show such optical phase distribution.

Two classical techniques are widely used to image phase objects: phase contrast methods [1–3] and interferometry [16]. With modern development of electronic devices such as detectors, for instance CCD sensors, digital holography has become in a practical powerful tool for analysis and quantification of phase samples [4–10]. In particular, a highly attractive interferometric configuration, named as common-path interferometry (CPI), provides significantly increased environmental stability and decreased system complexity in comparison with other interferometric architectures. CPI setup can be viewed as a classical Mach–Zehnder configuration with the particularity that both imaging and reference beams share the same optical path. CPI is a well-known technique mainly proposed to perform phase disturbances visualization [16–20]. On its classical configuration [16–18,20–22], a *4F* imaging processor allows access to the system's Fourier plane where a certain spatial filter, ranging from a diffraction grating to a nonlinear medium, is placed. Such spatial filter is used to convert the phase distribution at the *4F* imaging processor output plane into image contrast and, as a consequence, the phase distribution of the object under test is visualized.

But the previous methods [16–20] do not provide phase values of the two-dimensional (2-D) imaged phase distribution: they only show a qualitative analysis of the 2-D phase disturbance. To allow phase quantification and then to have access to the 3-D profile of the sample, we need to perform either off-axis holographic recording [4–5,8–10] or phase-shifting recording [6,21–22] between both interferometric beams. In particular, phase-shifting procedure [23–24] uses both an in-line recording setup to increase the fringe spacing and phase-shifting of the reference beam to evaluate directly the complex amplitude at the CCD plane and to completely eliminate the conjugates images.

In this paper, we first present an extremely simple experimental setup in CPI configuration useful to recover the sample's complex amplitude distribution by applying phase-shifting method. To do this, we divide the input plane into two contiguous regions in a similar way than in Ref. [20–22] and we place a Ronchi ruling grating in the proximity of the system's Fourier plane. In our setup we

* Corresponding author.
E-mail addresses: Vicente.mico@uv.es, vmico@aido.es (V. Mico).

0030-4018/$ - see front matter © 2008 Elsevier B.V. All rights reserved.
doi:10.1016/j.optcom.2008.04.079

shift the usability of the system to microscopy fields, by using a microscope objective as imaging system instead of thin lenses as in all the previous references [16–22]. So, the proposed approach is experimentally validated in DHM field where different microscope lenses with different NA values are compared. After that, the capabilities of the presented configuration are investigated in the field of superresolution when low NA microscope lenses are used. Let us now introduce a few lines providing a general background on time multiplexing superresolution to better define the scope the paper.

It is well known that the resolving power of imaging systems is limited by three main factors: diffraction, finite size of the detector pixel and noise [25]. Thus, the resolution limit of an imaging system imposed by diffraction can be defined as proportional to the wavelength (λ) of the illumination light and inversely proportional to its NA [26]. In other words, each imaging system provides a cut-off frequency in the Fourier domain (defined from its NA and the illumination λ) which limits the spatial-frequency content of the object's image providing a limited resolution image. In that sense, the aim of superresolution effect can be understood as the generation of a synthetic aperture that expands up the cutoff frequency of the imaging system [27–40]. The improvement is performed without any physical changes in the imaging optical system itself: it is done by encoding–decoding the optical information in the input object taking into account analysis of degrees of freedom provided by information theory [41–43] and *a priori* knowledge about the object [44–45].

In that sense, we had extended the usage of CPI to the field of time multiplexing far-field superresolution in DHM [34]. The CPI architecture was performed by placing a reference grating in part of the field of view in the object plane, that is, in side-by-side configuration with the object at the input plane. Thus, providing collimated off-axis illumination onto the input plane, both additional frequency band-passes of the object's spectrum and a reference beam are diffracted on-axis towards the microscope lens passing through it. After that, the additional frequency band-pass is recovered using off-axis holographic recording at the image plane performed by a second grating. However, a higher carrier frequency is needed at the CCD plane to avoid overlapping of the different hologram diffraction orders just to allow the recovery of the object's complex amplitude band-pass. Now, our new proposed setup improves the performance of the experimental configuration presented previously in Ref. [34] due to the use of phase-shifting instead of off-axis recording. Because the limitation of off-axis methods comes from the spatial separation of diffraction orders, phase-shifting in on-axis recording permits the use of the whole frequency plane. Thus, the overall reconstructed image is no longer limited by the presence of the zero diffraction order and its conjugate image. As no carrier frequency is needed, the space-bandwidth product of the imaging system is optimized with respect to the bandwidth of the recorded band-pass.

In the two parts of this paper, that is, experimental validation of the proposed setup and its extension to superresolution, the quantification of the object's phase distribution implies 3-D information of it. As the object used in the first paper part is a real planar object (USAF test), no 3-D profile is needed. On the other hand, for a biosample superresolution, the quantified superresolved phase distribution allows 3-D representation of the sample under test (where the z-axis is connected to the thickness of the sample).

The paper is organized as follows. Sections 2 and 3 provide a qualitative and mathematical analysis of the proposed setup, respectively. Section 4 shows experimental results for a planar USAF resolution test target and three different microscope objectives in order to validate the proposed approach in DHM. After that, Section 5 includes an experimental validation of the presented setup where DHM superresolution is obtained using a phase object biosample. And finally, Section 6 concludes the paper.

2. Optical experimental configuration: an intuitive interpretation

The basic optical system setup is depicted in Fig. 1 where a single on-axis point source (vertical cavity surface emitting laser – VCSEL) is used as divergent spherical illumination in the experimental setup. Two contiguous regions placed in side-by-side configuration compose the input plane. For the first part of the presented paper, the input plane is composed by the sample under test (USAF target) and a hollow area (white square in Fig. 1) at its left side. In this configuration, a microscope lens images the input plane amplitude distribution onto a CCD. Placed after the microscope lens, a one-dimensional (1-D) grating (named from now on as *imaging grating*) allows the digital holographic recording by mixing both reference and imaging beams at the CCD plane.

Unlike in Ref. [34], now the imaging grating is placed at the image plane of the point source through the microscope lens (Fig. 2), that is, at the system Fourier plane. This fact means that no carrier frequency is produced at the CCD plane during the holographic recording process. Then, when the imaging grating is not placed just at the Fourier plane, it provides a virtual source placed out of the optical axis for each one of its diffraction orders. Fig. 2 depicts this situation while considering three diffraction orders. Moreover, due to the spherical divergent illumination instead of

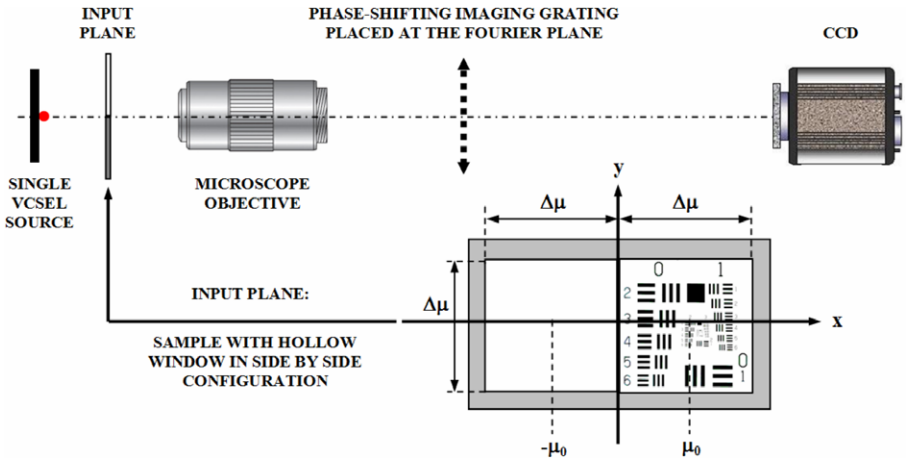

Fig. 1. Proposed common-path phase-shifting interferometric setup.

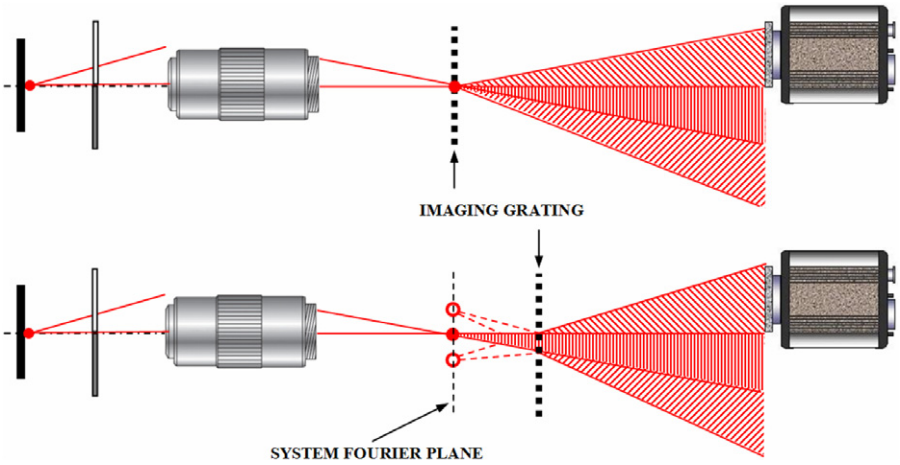

Fig. 2. Conceptual difference between the proposed experimental setup and Ref. [34]. The red circles at the Fourier plane represents the virtual sources provided by the fact that the imaging grating is not placed at the system Fourier plane and has three diffraction orders. (For interpretation of the references in colour in this figure legend, the reader is referred to the web version of this article.)

collimated one [34], the system Fourier plane is moved far from the microscope lens in comparison with the position of such plane when collimated illumination is used (back focal point of the lens). However, as the NA of the microscope lens increases, the distance from the lens rear mount to the Fourier plane decreases. This means that the proposed setup has a final limitation regarding the NA of the imaging lens in order to place the imaging grating just at the Fourier plane. Let us call such limit as *NA threshold value*. After such NA threshold value, the imaging grating will provide interferometric fringes at the CCD plane in a similar way than in Ref. [34]. But for low and medium NA microscope objectives, the proposed setup is still valid because of the imaging grating is placed at or near the Fourier plane. But even in the latter case, the generated fringe pattern is still resolved by the CCD pixel size.

In this configuration, by placing the CCD just at the position where direct object imaging is produced (no deviation by the imaging grating is introduced) and by properly selection of the imaging grating period, zero order imaging beam and first order reference beam overlap. The situation is depicted in Fig. 3. Then, if no moving parts are considered, a digital in-line hologram is recorded at the CCD. But applying subperiod shifts to the imaging grating, the overall phase of the recorded hologram changes. And this is the aim of phase-shifting methods. By placing the imaging grating onto a linear motion stage, we can move it and record a set of holograms with known phase step in order to apply standard reconstruction algorithms to recover complex amplitude distribution of the object under test.

For the superresolution validation of the proposed setup, two considerations must be introduced in the experimental setup shown in Fig. 1. First, a diffraction grating (named as *reference grating*) is placed at the input plane in the object's contiguous window. The aim of the reference grating is to provide on-axis diffracted reference beam for the holographic recording when off-axis illumination will be considered. And second, the single VCSEL source is laterally displaced in order to provide sequential off-axis illumination at proper angles. Notice that this fact is not a restriction

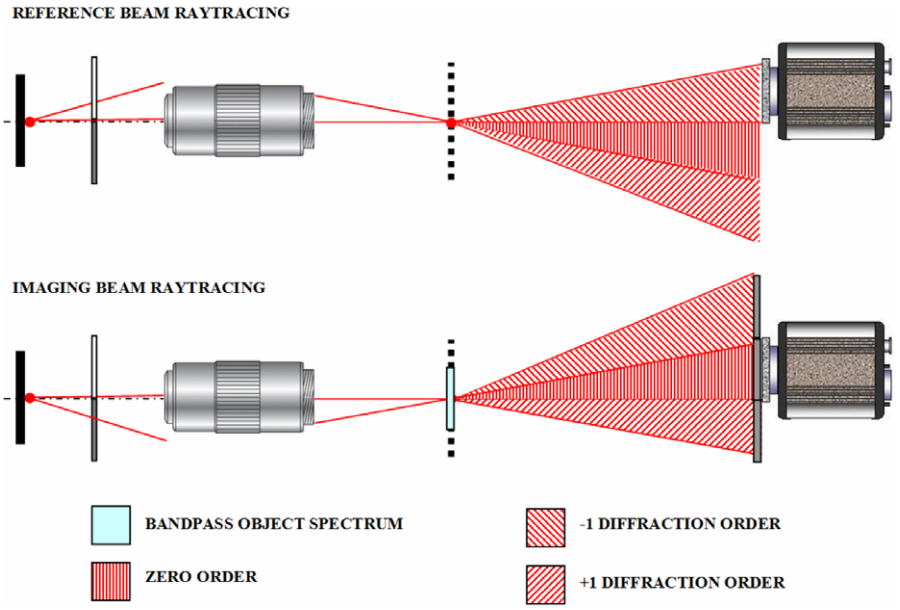

Fig. 3. Reference and imaging beam ray tracings in the proposed setup. At the CCD, -1 diffraction order and zero order for reference and imaging beam respectively performs holographic recording.

because a 2-D VCSEL array can be used matching the specifications needed. In that sense, the presented approach performs superresolution by time multiplexing (the process is performed in sequential mode) and with field of view restrictions (part of the input plane is occupied by the reference grating).

In our superresolution experiment, we use a 1-D grating as reference grating and by rotating it, we ensure on-axis reference beam for each oblique illumination angle when 2-D frequency space coverage is aimed for. As off-axis illumination shifts the object's spectrum, an imaging beam carrying an additional spatial-frequency band is now diffracted on-axis and can pass through the system aperture. The only condition to fulfill is that the oblique illumination angle is well adjusted with the NA of the microscope lens and the basic frequency of the reference grating. Similar phase-shifting recording process than that performed when on-axis illumination is considered allows the recovering of such additional frequency band-pass of the object's spectrum. Thus, it is possible to extend up the cutoff frequency of the limited system aperture after applying a digital post processing stage in which each one of the 2-D recovered frequency bands are assembled into one. This means the generation of a synthetic aperture that expands the 2-D frequency space coverage of the microscope lens. Finally, a superresolved image can be recovered by simple Fourier transformation of the previously generated synthetic aperture.

3. Mathematical analysis of the optical setup

In order to provide a simple theoretical analysis, the optical system depicted in Fig. 4 is considered. Notice that the only difference between setups shown in Figs. 1 and 4 is the image magnification of the microscope lens. Also, a 2-D VCSEL array representing all the possible off-axis illuminations and a reference grating having diffraction orders for every oblique illumination are considered just to describe a generalized setup. In this configuration, spherical point illumination incoming from a 2-D VCSEL source array illuminates the input plane in sequential mode. Eq. (1) provides the amplitude distribution at the input plane after being illuminated with a given spherical source that is originated at a point of coordinates (x_S, y_S) of the source plane and at z-distance in front of the input plane [34]

$$U_{IP}(x,y) = \left[t(x,y)\,rect\left(\frac{x-\mu_0}{\Delta\mu}, \frac{y}{\Delta\mu}\right) + \sum_{n,m} C_n C_m \exp\{-j2\pi v_0(nx+my)\}\, rect\left(\frac{x+\mu_0}{\Delta\mu}, \frac{y}{\Delta\mu}\right)\right] A \times \exp\left\{-j\frac{k}{2z}\left[(x-x_S)^2+(y-y_S)^2\right]\right\} \quad (1)$$

being $t(x,y)=|t(x,y)|\exp(i\varphi_0(x,y))$ the object's complex amplitude distribution function defined from $|t(x,y)|$ and $\varphi_0(x,y)$ as its real amplitude and phase distributions respectively, (x,y) the spatial coordinates, k is the wave number of the illumination wavelength, (n, m) the diffraction orders of the 2-D generalized reference grating, (C_n, C_m) and v_0 are the amplitude coefficients and the basic frequency of the 2-D reference grating in both x and y-directions, respectively. *rect* is the rectangle function that limits the sizes of the object and the reference grating positioned at the input plane as it can be seen in Fig. 1. Obviously, the rectangle that limits the extension of the input object is centered at μ_0 position while the corresponding to the reference grating is placed at $-\mu_0$ *position (both have the same* $\Delta\mu$ height and width).

Then, the first lens in Fig. 4 performs Fourier transformation of the input amplitude distribution onto its focal image plane, where a 1-D imaging grating is placed. The amplitude distribution at the system Fourier plane equals to

$$U_{FP}(u,v) = FT\{U_{IP}(x,y)\}\, circ\left(\frac{\rho}{\Delta v}\right) \sum_p B_p \exp\{j2\pi p v' u\} \quad (2)$$

where (u,v) are the spatial-frequency coordinates, ρ is the polar coordinate in the frequency domain that is defined as $\rho=\sqrt{u^2+v^2}$. The *circ* function represents the limited system's aperture with a width of Δv, and (B_P, v') are the amplitude coefficient and the basic frequency of the imaging grating, respectively. After that, a second Fourier transformation is performed between the Fourier plane and the output plane. Leaving aside constant factors, the final amplitude distribution at the output plane is proportional to

$$U_{OP}(x',y') = U_{IP}(-x',-y') \otimes disk(\Delta v\, r) \otimes \sum_p B_p \delta(x' - p\lambda F v') \quad (3)$$

being *disk* $(\Delta v,\ r)$ the point spread function (PSF) of the *4F* processor defined from the first order Bessel function as $\text{disk}\ (\Delta v r) = \frac{J_1(2\pi\Delta v r)}{\Delta v r}$, r the polar coordinate that is defined as $r=\sqrt{x'^2+y'^2}$, and λF the scale factor of the second Fourier transformation.

As in Ref. [34], we must properly adjust the off-axis positions (x_S, y_S) of the point sources with the basic frequency (v_0) of the reference grating and with the radius (Δv) of the system's aperture. Assuming this is accomplished (see Ref. [34]), the most important fact in Eq. (3) is the last convolution with the delta function incoming from the imaging grating. This convolution means that the transmitted band-pass image is replicated at the output plane. To allow correct overlapping between imaging and reference beams, it is necessary that

$$v' = \frac{2\mu_0}{\lambda F} \quad (4)$$

that is, the separation between the replicas generated by the imaging grating at the output plane must be equal to the separation between the two regions that compose the input plane. In the case of using a microscope lens instead of a unit magnification imaging system, the magnification power or the microscope lens must be taken into account. In any case, Eq. (4) defines the basic frequency of the 1-D imaging grating.

In this configuration and as it can be seen from Fig. 3, the CCD images an on-axis hologram where no bias carrier frequency between both interferometric beams is generated. In order to recover both amplitude and phase distributions of the transmitted frequency band-pass, a phase-shifting method is applied. Concep-

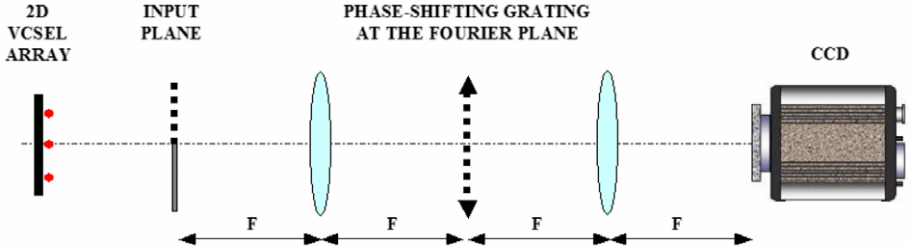

Fig. 4. Simplified optical setup used to analyze the mathematical foundation of the presented approach.

tually and under these conditions, the intensity distribution recorded at the CCD at a given instant t and due to a generic point source originated at (x_S, y_S) position comes from the addition of the imaging beam (band-pass image selected by such source convolved with the PSF of the imaging system) and an on-axis reference beam due to the imaging grating

$$I_{OP}(x',y',t) = \left| \left(t(-x',-y') e^{j\frac{2\pi}{\lambda z}[x_S x' + y_S y']} \right) \otimes disk(\Delta v, r) + C e^{j[\phi_S(x,y)+\phi_m(t)]} \right|^2 \tag{5}$$

being C a constant related to the real amplitude of the reference beam, ϕ_S the initial phase difference between imaging and reference beams which is directly related with the transmitted phase distribution of the object due to the source placed at (x_S, y_S), and ϕ_m the linear phase increment introduced in time between two subsequent intensity images. Notice that linear phase variation in time is assumed and the spherical phase factor, common to both interferometric terms and related with the divergence of both beams, has been removed. Also, as the object's amplitude distribution function $t(x,y)$ is complex, both amplitude and phase distributions of the input object are limited by the PSF of the imaging lens.

As the time dependence of the recorded intensity can be expressed as a function of the intensity image number m multiplied by the phase step between two consecutive images ($\varphi_m = m\varphi_K$) and taken the different intensity distributions in time sequence, Eq. (5) can be rewritten as

$$\begin{aligned} I^m_{OP}(x',y',t_m) &= \left| \left(t(-x',-y') e^{j\frac{2\pi}{\lambda z}[x_S x' + y_S y']} \right) \otimes disk(\Delta v, r) \right|^2 + C^2 \\ &+ C\left[\left(t(-x',-y') e^{j\frac{2\pi}{\lambda z}[x_S x' + y_S y']} \right) \otimes disk(\Delta v r) \right] e^{-j[\phi_S(x,y)+m\phi_k]} \\ &+ C\left[\left(t(-x',-y') e^{j\frac{2\pi}{\lambda z}[x_S x' + y_S y']} \right) \otimes disk(\Delta v, r) \right]^* e^{j[\phi_S(x,y)+m\phi_k]} \\ &= A(x,y) + B(x,y)\cos(\phi_S(x,y) + m\phi_k) \end{aligned}$$

where $A(x, y)$ is representative of the object image intensity plus a constant given by the reference beam, and $B(x, y)$ is coming from the real part of the object amplitude distribution

$$\begin{aligned} A(x,y) &= \left| \left(t(-x',-y') e^{j\frac{2\pi}{\lambda z}[x_S x' + y_S y']} \right) \otimes disk(\Delta v r) \right|^2 + C^2 B(x,y) \\ &= 2CRe\left[\left(t(-x',-y') e^{j\frac{2\pi}{\lambda z}[x_S x' + y_S y']} \right) \otimes disk(\Delta v r) \right] \end{aligned} \tag{7}$$

Then, by using phase-shift algorithm and computing the different intensity distributions stored by the CCD, it is possible to recover each transmitted phase distribution $\phi_S(x,y)$ of the input object due to each (x_S, y_S) illumination source [15]. In particular, we have applied a method that takes into account m intensity images in one phase-shift period and permits the recovering of the initial phase distribution according to

$$\phi_S(x,y) = \mathrm{Arg}\left\{ \sum_{i=1}^{m} I_i(x,y) \exp\left[-j\frac{2\pi}{m}(i-1) \right] \right\} \tag{8}$$

This procedure allows us to recover the phase distribution, and therefore the object's complex amplitude, of each one of the frequency bands transmitted through the system's aperture when illumination incoming from the position (x_S, y_S) in the 2-D VCSEL array is considered. For validating the proposed setup as common-path phase-shifting DHM, only on-axis illumination provided by a point source placed at $(x_S, y_S) = (0, 0)$ is considered.

On the other hand and for the superresolution implementation, different off-axis source positions must be lighted on in sequential mode and every frequency band-pass must be sequentially recovered. After that and by properly placing them on its original position, a wider spectral content of the object can be fully reconstructed in terms of synthetic aperture generation. Thus, provided that there will be a diffraction order in the 2-D reference grating for each 2-D VCSEL source position, any synthetic aperture can be shaped.

4. Experimental results: validation of the proposed setup

In order to check the capabilities of the presented experimental setup, different commercial microscope objectives have being used in the proposed configuration. We present images for three different microscope lenses: a 0.1NA Nikon lens, and a 0.28NA and 0.42NA long working distance infinity corrected Mitutoyo lenses. A VCSEL source array with ($\lambda = 850$ nm, ±15° beam divergence) provides on-axis illumination for the experiments. The central high-resolution part of a positive USAF test target is used to compare the results. Fig. 5 depicts, for each microscope lens, a set of 4 holographic images obtained using a CCD camera (Kappa DC2, 12 bits, 1352×1014 pixels with 6.7 μm pixel size). As imaging grating, we used a 1-D Ronchi ruling grating (80 lp/mm) and it is placed on a motorized linear translation stage. Then, a displacement on the grating of 12.5 μm implies a complete phase cycle in the recorded hologram.

The grating motion steps produced in the image sequence presented in Fig. 5 correspond with a shift of 3.125 μm between two consecutive images. In this case, the imaging grating displacement is equivalent to a phase step of $\pi/2$ radians. As the imaging grating can be placed just at the Fourier plane in the first two cases, we can see that the recorded holograms have no carrier frequency. But this is not the case of the 0.42NA lens where the Fourier plane is inside the microscope objective itself. In this case, the imaging grating was placed in close contact with the microscope lens and, even so, a fringe pattern is still obtained for the sequence of recorded holograms.

Now, if we take a look in the Fourier domain of one hologram for each lens case (see Fig. 6), we will see that, for the two first cases, the zero order term and the two holographic images are centered at the Fourier domain and overlaps. In the case of the 0.42NA lens, the resulting fringe pattern introduces a carrier frequency that shifts the diffraction orders. So, phase-shifting method is still needed to recover complex amplitude distribution of the object. For a given range of higher NA lenses, the diffraction orders will be non-overlapping and holographic recording in off-axis mode will be produced. In such case, there is no need to apply phase-shifting because the first diffraction order can be filtered and the object's complex amplitude distribution obtained (this is the case of Ref. [34]).

5. Experimental results on superresolution of phase samples

With the modifications that were previously commented in Section 2, the proposed common-path phase-shifting interferometric setup is investigated for superresolution imaging purposes. We select as object a biosample of fixed human red blood cells. The erythrocytes slide is stained using a specially prepared mixture of methylene blue and eosin in methanol (Wright stain). Once again, a single VCSEL source placed onto a 2-D linear motion stage is used to illuminate the system. A low NA lens (0.1NA Nikon lens) is used to show the capabilities of the superresolution effect. Notice that using higher divergence sources, the procedure is suitable to be applied onto higher NA lenses whenever the condition that the imaging grating can be placed near the Fourier plane will be fulfilled.

In order to obtain a superresolution effect not only in the vertical and horizontal directions but in the full 2-D frequency space, the reference grating is rotated to match its orientation with the oblique illumination. As reference grating, we used a 1-D Ronchi ruling grating with a basic period of 5 μm (200 lp/mm). The

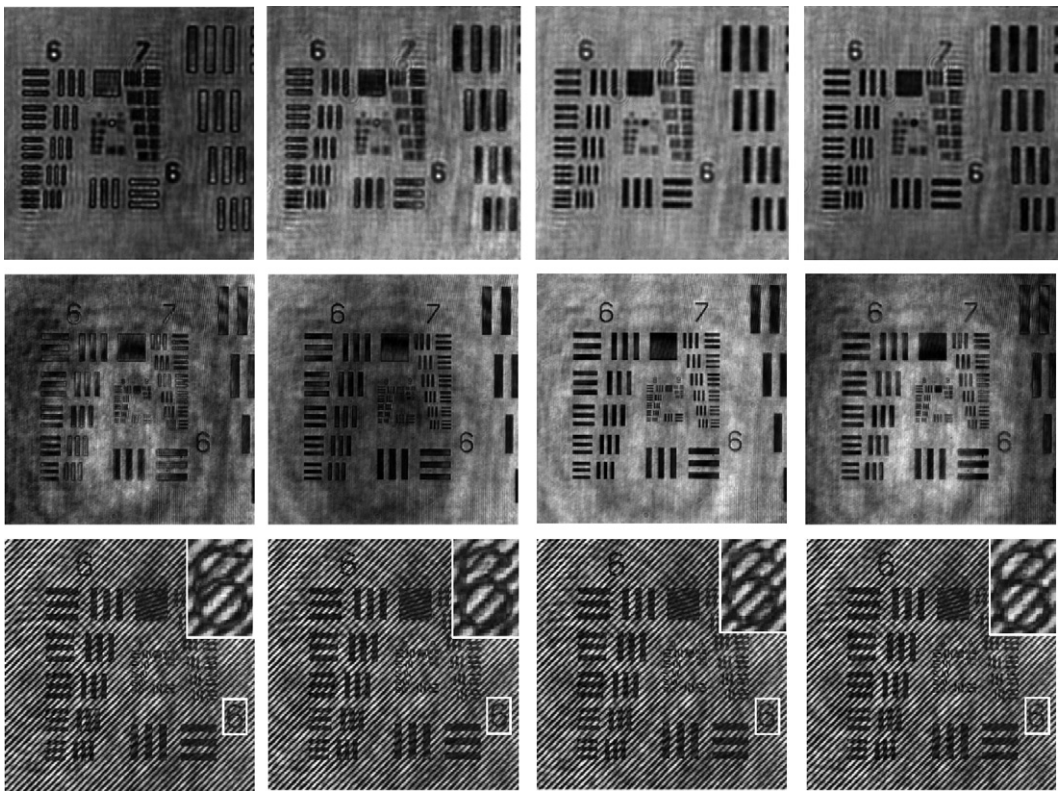

Fig. 5. CCD recorded holograms for 0.1NA (upper row), 0.28NA (medium row) and 0.42NA (lower row) microscope lenses. The phase-shifting effect can be seen from left to right images for each lens case. In the 0.42NA lens, the region marked with a white rectangle is enhanced to show the fringe shift between images.

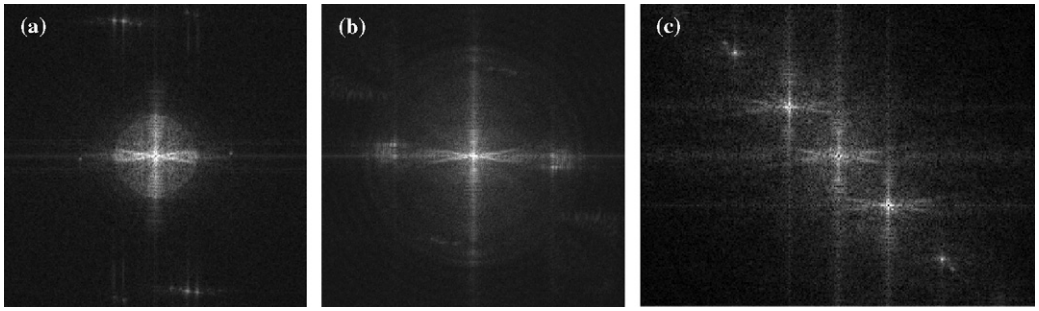

Fig. 6. Fourier transformation of the first image of each row in Fig. 5 for the three microscope lenses analyzed: (a) 0.1NA, (b) 0.28NA, and (c) 0.42NA. The DC terms in (c) have been blocked to enhance the image contrast.

off-axis illumination angles produced in our experiment was near 10° for every oblique incident direction. This means that a quasi-contiguous frequency band is on-axis diffracted through the system aperture because the angle defined by the NA of the microscope lens is 5.74° (that is, near the half angle of the off-axis illumination). So, a resolution gain factor close to 3 will be achieved in every off-axis illumination direction.

Phase-shifting process is achieved by storing holograms each with the phase-shift due to a linear shift of 0.5 μm. As the period of the imaging grating is 12.5 μm, 25 consecutive images (captured with the same CCD model than in that one used in Section 4) will be considered in a full cycle when phase-shifting algorithm is used to recover each one of the frequency band-passes. The exposure times for the different off-axis illuminations were 11 ms for the central band and 44 ms for the off-axis bands. Fig. 7 images the eight off-axis frequency bands recovered after apply phase-shifting procedure (eight exterior rectangles marked with white line) and the SA (central part) that is generated by replacing the different frequency bands. Obviously, a central band-pass is also recovered using on-axis illumination.

As the tilted illumination angle is not twice the half angle defined by the NA of the lens, the off-axis frequency bands will contain a portion of the central one. We should note this fact due to the high intensity region at the adjacent border in all the single elementary pupils depicted in Fig. 7 with respect the central frequency band. This overlapping avoids the achievement of a resolution gain factor of 3 but allows the full 2-D frequency space coverage without remaining of any uncovered regions between the different frequency bands.

The replacement of each elementary pupil to its original position in the object's spectrum is performed in two basic steps. First, by measuring the illumination angle of each tilted beam (initial calibration stage), we know the general shift that must be applied at the Fourier domain to each elementary pupil in order to bring back. And second, fine linear phase factor addition over each single pupil allows a final accurate adjustment of the position of each ele-

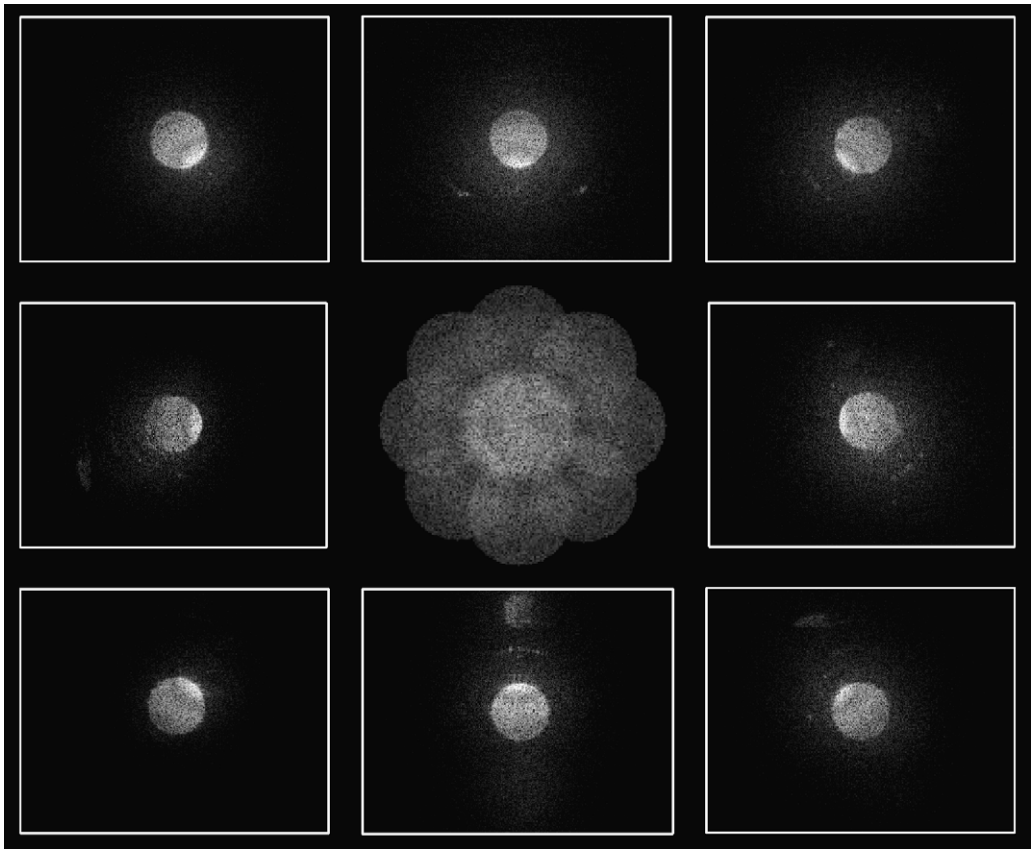

Fig. 7. The eight off-axis frequency bands (exterior rectangles) and the synthesized extended aperture (central part of the image).

mentary pupil in the synthesis of the SA. Notice that no equalization is performed between the different recovered frequency bands: the synthetic aperture is the addition of the nine single pupils. Thus, a final high quality superresolved image is obtained by Fourier transformation of the information contained in the SA. Fig. 8 shows the superresolved images in comparison with the

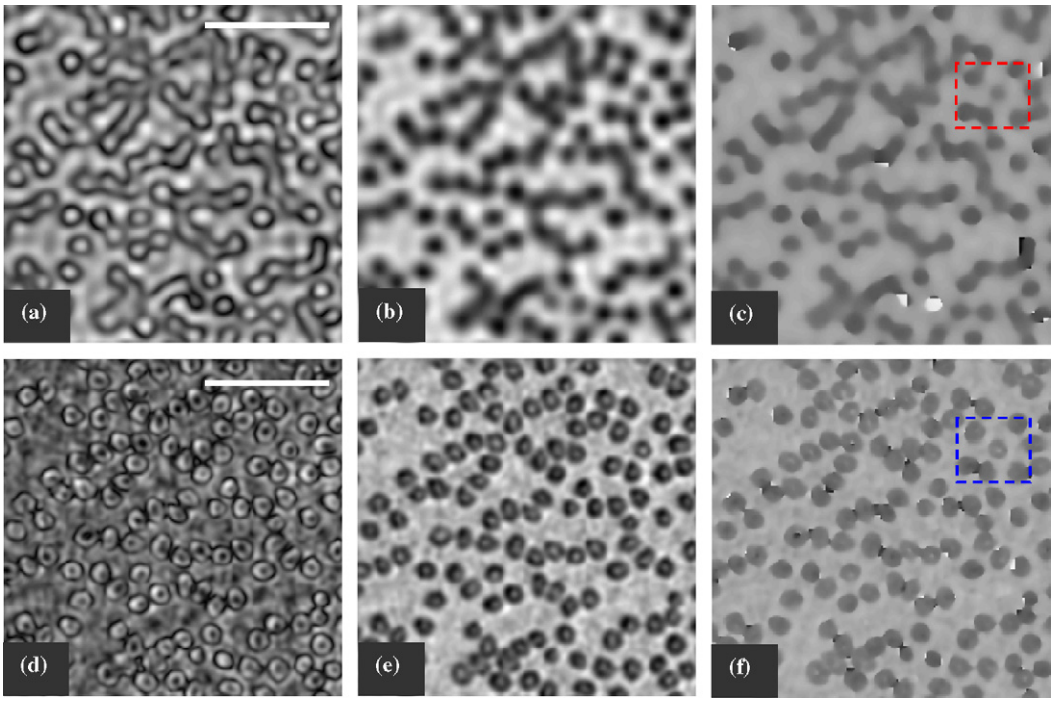

Fig. 8. (a) Low-resolution complex amplitude image recovered using phase-shifting and on-axis illumination, and (b) and (c) its real part and phase distributions, respectively. (d) Superresolved complex amplitude image using the proposed approach, and (e) and (f) its superresolved real part and phase distributions, respectively. The white scale bars in (a) and (d) are 50 μm.

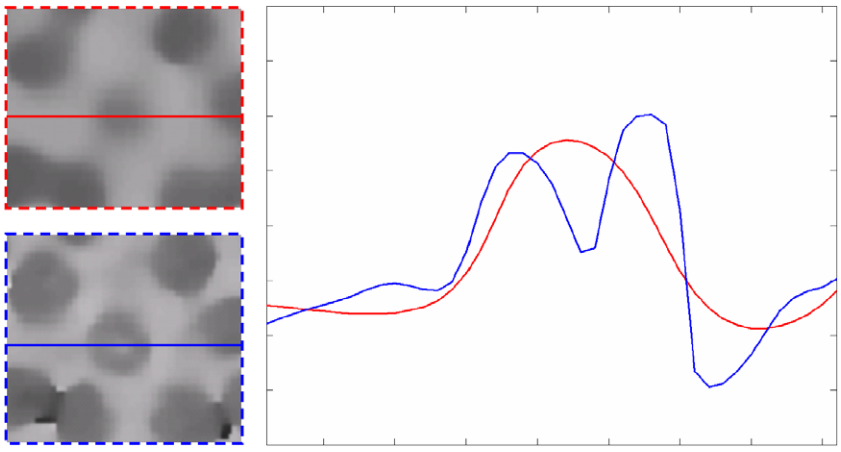

Fig. 9. Unwrapped phase plots corresponding with red and blue lines in Fig. 7c and f.

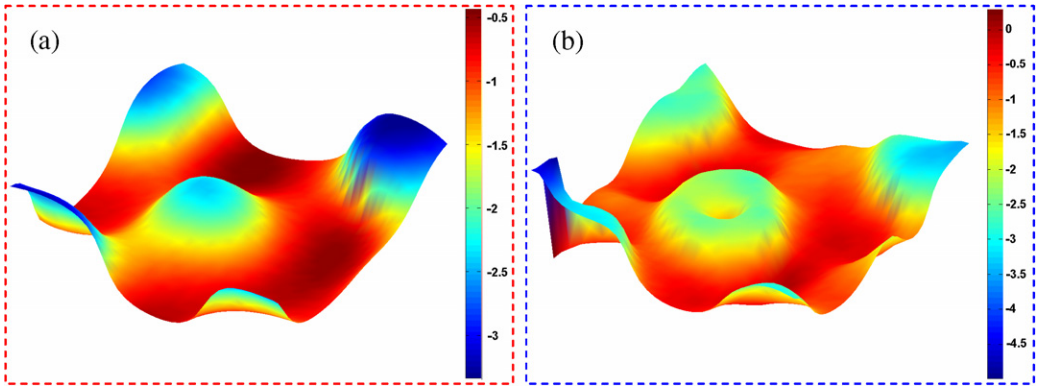

Fig. 10. 3-D representations of the unwrapped phases corresponding with red and blue lines in Fig. 7c and f for the cases of (a) low-resolution image and (b) superresolved image. Color bars represent optical phase in radians. (For interpretation of the references in colour in this figure legend, the reader is referred to the web version of this article.)

low-resolution ones. An impressive superresolution effect can be observed where one may see the thinner area in the center of each red blood cell. This area, observed as a black point, is originated by deviation of the light at the center of the cells due to the typical donut-like shape of the red blood cells.

Theoretically, the resolution limit of the 0.1NA lens is 8.5 μm for the 850 nm wavelength. According to the size of the red blood cells (between 6 and 8 μm in diameter), this resolution capability it is not high enough to visualize the biosample [see Fig. 8a]. Moreover, the cells are on the resolution limit of the microscope lens. Due to the off-axis illumination, the synthetic NA (SNA) generated using this approach is defined as $SNA = NA_{source} + NA_{objective} \cong 0.27$. This means that the theoretical resolution limit of the synthetic imaging system is 3.1 μm and it enables image formation of the cells [see Fig. 8d].

In our experimental configuration, the field of view that can be imaged at the input plane by the biosample is 0.6×0.45 mm while for normal imaging the field of view would be twice this size. This reduction comes from the need to cover the input plane by the reference grating.

Fig. 9[1] plots the unwrapped sections of the phase distributions corresponding with the red and blue lines of the dashed red and blue rectangles included in Figs. 8c and f. One may see as in the low-resolution phase distribution plot (red line), the slope of the plot is lower than in the high-resolution case (blue line). This means that the phase slope is steeper in the high-resolution case, that is, the phase distribution is also superresolved. Moreover, the central peak in the high-resolution plot represents the donut-like shape that cannot be appreciated in the low-resolution case. This effect is more evident in the images shown in Fig. 10 where a three-dimensional (3-D) representation of the unwrapped phase distribution is depicted for comparison between the low-resolution (conventional) image and the superresolved image obtained using the proposed approach. The represented areas are also the same ones considered in Fig. 9.

6. Conclusions

A new setup has been proposed that relies in the usage of an ultra-simple new configuration aimed to achieve phase-shifting in common-path interferometric configuration and applied to DHM as first time. The interferometric architecture has a minimum of optical elements in the experimental setup. Experimental validation suggests that the method can be applied for low and medium NA microscope lenses. The setup has the advantage that no high frequency pattern is produced at the detector plane (optimizing then the used space-bandwidth product of the detector) while the imaging grating could be placed close to the system Fourier plane. Then, phase-shifting method allows holographic recording

[1] (For interpretation of the references in colour in this figure legend, the reader is referred to the web version of this article.)

in or approximately on-axis mode. As a consequence, the experimental setup becomes easy-to-configure and it is useful for implementation in microscopes having low and medium NA lenses where only simple modifications are required.

The fact that the illumination used in this paper is spherical rather than collimated has a double meaning. On one hand, it reduces the number of optical elements simplifying the final experimental setup. And on the other hand, it allows the usage of not only low NA lenses but also medium NA ones because the system's Fourier plane is shifted back the microscope lens in comparison with its position using collimated illumination.

In a second part, the proposed approach has being tested under superresolution aims. While in Ref. [34] we had used a synthetic object (USAF test target) to show the resolution improvement, in the presented paper we have used phase objects (human red blood cells) as biosample. This fact validates the new approach, as well as Ref. [34], to provide 3-D quantitative retrieval of phase objects.

Although a circular synthetic aperture is experimentally demonstrated by rotating the 1-D reference grating, it is possible to generate any synthetic aperture shape by substituting the 1-D reference grating by a 2-D one with the appropriate grating frequencies depending on the aimed aperture. In that sense, if a 2-D holographic grating is placed at the input plane (as in Ref. [34]), cross-shaped pupil and square aperture can be generated by providing cross-shape and square shape off-axis illumination beams onto the input plane, respectively.

In the presented superresolution validation, off-axis illumination allows the transmission through system's aperture of new additional frequency band-passes that are not transmitted in a conventional illumination mode. The oblique illumination is performed using a single VCSEL element which is moved to off-axis positions. This procedure is equivalent to having an array of coherent sources that are incoherent one with each other. This VCSEL array allows recording of each band-pass in a short time due to its high optical power per every emitter. Additionally, the digital post processing associated with the generation of the superresolved image is simple and fast, as it only requires simple and linear digital operations.

Other advantages of the proposed setup come from the common-path interferometric architecture; the imaging and the reference beams follow nearly the same optical path providing to the experimental setup two main advantages: On one hand, the instabilities of the system, due to mechanical or thermal changes on both optical paths, do not affect the obtained results. On the other hand, low coherence length light sources are suitable to be used as illumination.

Acknowledgements

The authors want to thank Professor Francisco Javier Perucho Lizcano for the human red blood cells biosample preparation. Also, part of this work was supported by the Spanish Ministerio de Educación y Ciencia and FEDER funds under the Project FIS2007-60626.

References

[1] F. Zernike, Physica 9 (1942). Part I, p. 686; Part II, p.974.
[2] F. Zernike, Science. 121 (1955) 345.
[3] J. Glückstad, Opt. Commun. 130 (1996) 225.
[4] E. Cuche, F. Bevilacqua, Ch. Depeursinge, Opt. Lett. 24 (1999) 291.
[5] G. Popescu, T. Ikeda, R.R. Dasari, M.S. Feld, Opt. Lett. 31 (2006) 775.
[6] H. Medecki, E. Tejnil, K.A. Goldberg, J. Bokor, Opt. Lett. 21 (1996) 1526.
[7] H. Elfström, A. Lehmuskero, T. Saastamoinen, M. Kuittinen, P. Vahimaa , Opt. Exp. 14 (2006) 3847.
[8] A. Anand, V.K. Channiwal, Appl. Opt. 46 (2007) 2022.
[9] F. Charrière, J. Kühn, T. Colomb, F. Montfort, E. Cuche, Y. Emery, K. Weible, P. Marquet, Ch. Depeursinge, Appl. Opt. 45 (2006) 829.
[10] T. Colomb, J. Kühn, F. Charriere, Ch. Depeursinge, Opt. Exp. 14 (2006) 4300.
[11] H. Hinrichs, K.D. Hinsch, J. Kickstein, M. Böhmer, Opt. Lett. 22 (1997) 828.
[12] G. Pang, H. Meng, Appl. Opt. 42 (2003) 827.
[13] B. Kern, P.E. Dimotakis, Ch. Martin, D.B. Lang, R.N. Thessin, Appl. Opt. 44 (2005) 7424.
[14] R. Anderson, J. Milton, C. Anderson, Common Path Interferometers for Flow Visualization: A Review, AIAA 95-0481, American Institute of Aeronautics and Astronautics, New York, 1995.
[15] T. Kreis, Handbook of Holographic Interferometry: Optical and Digital Methods, Wiley-VCH Verlag GmbH & Co. KGaA, Weinheim, 2005.
[16] H. Kadono, N. Takai, T. Asakura, Appl. Opt. 26 (1987) 898.
[17] Ch.S. Anderson, Appl. Opt. 34 (1995) 7474.
[18] J. Glückstad, P.C. Mogensen, Appl. Opt. 40 (2001) 268.
[19] C.G. Teviño-Palacios, M.D. Iturbe-Castillo, D. Sánchez-de-la-Llave, R. Ramos-García, L.I. Olivos-Pérez, Appl. Opt. 42 (2003) 5091.
[20] V. Arrizón, D. Sánchez-de-la-Llave, Opt. Lett. 29 (2004) 141.
[21] C. Meneses-Fabian, G. Rodriguez-Zurita, J.F. Vazquez-Castillo, C. Robledo-Sanchez, V. Arrizón, Opt. Commun. 264 (2006) 13.
[22] C. Meneses-Fabian, G. Rodriguez-Zurita, V. Arrizón, J. Opt. Soc. Am. A 23 (2006) 298.
[23] I. Yamaguchi, T. Zhong, Opt. Lett. 22 (1997) 1268.
[24] I. Yamaguchi, J. Kato, S. Ohta, J. Mizuno, Appl. Opt. 40 (2001) 6177.
[25] Z. Zalevsky, D. Mendlovic, Optical Super Resolution, Springer, 2002.
[26] E. Abbe, Arch. Mikrosk. Anat. 9 (1873) 413.
[27] V. Mico, Z. Zalevsky, P. García-Martínez, J. García, Opt. Express 12 (2004) 2589.
[28] X. Chen, S.R.J. Brueck, Opt. Lett. 24 (1999) 124.
[29] M.G.L. Gustafsson, J. Microsc. 198 (2000) 82.
[30] R. Heintzmann, P.A. Benedetti, Appl. Opt. 45 (2006) 5037.
[31] C.J. Schwarz, Y. Kuznetsova, S.R.J. Brueck, Opt. Lett. 28 (2003) 1424.
[32] J. García, Z. Zalevsky, D. Fixler, Opt. Express 13 (2005) 6073.
[33] V. Mico, Z. Zalevsky, P. García-Martínez, J. García, Appl. Opt. 45 (2006) 822.
[34] V. Mico, Z. Zalevsky, J. García, Opt. Express 14 (2006) 5168.
[35] V. Mico, Z. Zalevsky, P. García-Martínez, J. García, J. Opt. Soc. Am. A 23 (2006) 3162.
[36] Y. Kuznetsova, A. Neumann, S.R.J. Brueck, Opt. Express 15 (2007) 6651.
[37] S.A. Alexandrov, T.R. Hillman, T. Gutzler, D.D. Sampson, Phys. Rev. Lett. 97 (2007) 168102.
[38] J.R. Price, P.R. Bingham, C.E. Thomas Jr., Appl. Opt. 46 (2007) 826.
[39] G. Indebetouw, Y. Tada, J. Rosen, G. Brooker, Appl. Opt. 46 (2007) 993.
[40] V. Mico, Z. Zalevsky, J. García, Opt. Commun. 276 (2007) 209.
[41] G. Toraldo di Francia, J. Opt. Soc. Am. 59 (1969) 799.
[42] I.J. Cox, J.R. Sheppard, J. Opt. Soc. Am. A 3 (1986) 1152.
[43] C.J.R. Sheppard, K.G. Larkin, Optik 113 (2003) 548.
[44] W. Lukosz, J. Opt. Soc. Am. 56 (1966) 1463.
[45] W. Lukosz, J. Opt. Soc. Am. 57 (1967) 932.